

Learning Higher-Order Dynamics in Video-Based Cardiac Measurement

Brian L. Hill¹, Xin Liu², and Daniel McDuff³

¹ University of California, Los Angeles, CA, USA
`brian.l.hill@cs.ucla.edu`

² University of Washington, Seattle, WA, USA
`xliu0@cs.washington.edu`

³ Microsoft Research, Redmond, WA, USA
`damcduff@microsoft.com`

Abstract. Computer vision methods typically optimize for first-order dynamics (e.g., optical flow). However, in many cases the properties of interest are subtle variations in higher-order changes, such as acceleration. This is true in the cardiac pulse, where the second derivative can be used as an indicator of blood pressure and arterial disease. Recent developments in camera-based vital sign measurement have shown that cardiac measurements can be recovered with impressive accuracy from videos; however, most of the research has focused on extracting summary statistics such as heart rate. Less emphasis has been put on the accuracy of waveform morphology that is necessary for many clinically meaningful assessments. In this work, we provide evidence that higher-order dynamics are better estimated by neural models when explicitly optimized for in the loss function. Furthermore, adding second-derivative inputs also improves performance when estimating second-order dynamics. We illustrate this, by showing that incorporating the second derivative of both the input frames and the target vital sign signals into the training procedure, models are better able to estimate left ventricle ejection time (LVET) intervals.

Keywords: Computer Vision, Dynamic Systems, Deep Learning, Optimization

1 Introduction

Many of the properties of dynamical systems only become apparent when they move or change as the result of forces applied to them. In most applications we are interested in behavior in terms of positions, velocities, and accelerations, and in some cases the properties of interest may only be observed in subtle variations in the higher-order dynamics (e.g., acceleration). Whether monitoring the flight of a drone to create a control mechanism for stabilization or analyzing the fluid dynamics of the cardiovascular system in the human body, there can be a need to recover these dynamics accurately. However, most video-based systems are trained on lower-order signals, such as position in the case of landmark tracking

or velocity/rate-of-change (optical flow) in the case of visual odometry [29]. Thus, they optimize for lower (zeroth or first) order dynamics. Does this harm their ability to estimate higher order changes? We hypothesize that networks trained to predict temporal signals will benefit from combined multi-derivative learning objectives. To test this hypothesis, we explore video-based cardiac measurement as an example application with a complex dynamical system (the cardiovascular system) and introduce simple but effective changes to the inputs and outputs to significantly improve the measurement of clinically relevant parameters.

Photoplethysmography (PPG) is a low-cost and non-invasive method for measuring the cardiovascular blood volume pulse (BVP). There are many clinical applications for PPG as the signal contains substantial information about health state and risk of cardiovascular diseases [11,36,33]. In the current world, an acutely relevant application of PPG is for pulse oximetry (i.e. measuring pulse rate and blood oxygen saturation) as it can be used to detect low blood oxygen levels associated with the onset of COVID-19 [16]. The COVID-19 pandemic has accelerated the adoption of telehealth systems [2] with more and more clinical consultations being conducted virtually. Therefore, techniques for remotely monitoring physiological vital signs are becoming increasingly important [14,37]. As one might expect, with many clinical applications the precision with which the PPG signal can be recovered is of critical importance when it comes to accurate inference of downstream conditions and the confidence of practitioners in the technology.

To date, in video-based PPG measurement the primary focus of analysis and evaluation has been on features extracted from the raw waveform or its first derivative [6,23,24,34,18]. However, the second derivative of the PPG signal highlights subtle features that can be difficult to discern from those in the lower derivatives. Since the second derivative reflects the acceleration [42] or the rate-of rate-of change of the blood volume, it is more closely related to the change in pressure applied by the heart on blood vessels and its relation to vascular health.

An example of a particular feature accentuated in the second-derivative (i.e. acceleration) PPG is the dicrotic notch (see Fig. 1), which occurs when the heart’s aortic valve closes due to the pressure gradient between the aorta and the left ventricle. The dicrotic notch may only manifest as an inflection in the raw PPG wave; however, in the second derivative this inflection is a maxima. [19] found that the second derivative of the PPG signal can be used as an indicator of arterial stiffness - which itself is an indicator of cardiac disease. [43] evaluated the second derivative of the PPG waveform and found that its characteristic shape can be used to estimate vascular aging, which was higher in subjects with a history of diabetes mellitus, hypertension, hypercholesterolemia, and ischemic heart disease compared to age-matched subjects without.

While the second derivative of a signal can be a rich source of information, often the zeroth- or first-order dynamics are given priority. For example, [6] observed that training video- or imaging-based PPG (iPPG) models using first-derivative (difference) frames as input with an objective function of minimizing the mean squared error between the prediction and the first derivative of the

target BVP signal was effective. This approach was used because the authors were designing their system to measure systolic time intervals only, which are most prominent in the lower order signals. However, they did not combine this with higher-order derivatives nor did they do any systematic comparison across derivative objectives.

We argue that a model trained with an explicit second-derivative (acceleration) objective should produce feature representations that better preserve/recover these dynamics than methods that simply derive acceleration from velocity. We observe that providing the model with a second derivative input also helps the network to better predict both the first and second derivative signals.

Finally, as diverse labeled data for training supervised models for predicting dynamical signals is often difficult to come by, we build on promising work in simulation to obtain our training data. Since light is absorbed and reflected differently for different skin tones [3,9] having a training set that represents the true diversity of the target population is crucial for sufficient generalization. Our results show that models trained with synthetic data can learn parameters that successfully generalize to real human subjects. While this is not a central focus of our paper, we believe that it presents a promising proof-of-concept for future work.

To summarize, in this paper, we 1) demonstrate that directly incorporating higher-order dynamics into the loss function improves the quality of the estimated higher-order signals in terms of waveform morphology, 2) show that adding second-derivative inputs additionally improves performance, and 3) we describe a novel deep learning architecture that incorporates the second derivative input frames and target signals and evaluate it against clinical-grade contact sensor measurements.

2 Background

Learning Higher-Order Motion from Videos. Despite its significance in many tasks, acceleration is often not explicitly modeled in many computer vision methods. However, there is a small body of literature that has considered how to recover [10] and amplify optical acceleration [52,44]. Given that acceleration can be equally as important as position and velocity in understanding dynamical systems, we argue that this topic deserves further attention.

A particularly relevant problem to ours is identifying small changes in videos [49,52,8,44], and specifically in acceleration in the presence of relatively large motion. As an example, in the iPPG prediction task the aim is to identify minor changes in skin coloring due to variation in blood flow patterns, while ignoring major pixel changes due to subject or background motion. One method proposed by [52] for overcoming this signal separation problem is Video Acceleration Magnification, in which large motions are assumed to be linear on the temporal scale while small changes deviate from this linearity. An extension to this method focused on making it more robust to sudden motions [44]. In both cases, a combination of Eulerian and Lagrangian approaches was used, rather than utilizing

a supervised learning paradigm. Of relevance here is also work magnifying subtle physiological changes using neural architectures [8], which have been shown to effectively separate signal and noise in both the spatial and temporal domains.

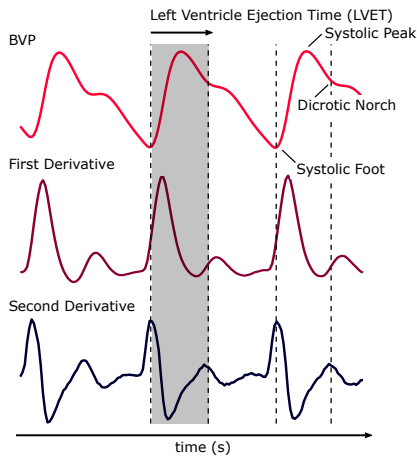


Fig. 1. The Left Ventricle Ejection Time (LVET) is the duration between the beginning and end of the systolic phase of the cardiac cycle. This interval corresponds to the opening and closing of the heart’s aortic valve, during which the left ventricle ejects blood into the system. In the PPG waveform, this interval begins at the diastolic point and ends with the dicrotic notch.

PPG signal [50,41,45,34]. The task then becomes separating pixel changes due to blood flow from those due to body motions, ambient lighting variation, and other environmental factors that we consider noise in this context. While earlier methods leveraged source separation algorithms [47], such as ICA [34] or PCA [22], neural models provide the current state-of-the-art in this domain [6,23,24,38,25]. These architectures support learning spatial attention and source-specific temporal variations and separating these from various sources of noise. Typically, the input to these models are normalized video frames and the output is a 1-D time series prediction of the PPG waveform or the heart rate. A vast majority of work has evaluated these methods based errors in heart rate estimation, which considers the dominant or “systolic” frequency alone. Only a few papers have used more challenging evaluation criteria, such as the estimation of systolic to diastolic peaks [27].

Our work might be most closely related to prior research into feature descriptors for optical acceleration [10]. One example uses histograms of optical acceleration to effectively encode the motion information. However, this work also defined handcrafted features, rather than learning representations from data. Our work is also related conceptually to architectures such as SlowFast [13] in that it utilizes multiple “pathways” to learn different properties of the dynamics within a video. We were inspired by this approach; however, unlike SlowFast, we focus specifically on higher-order pathways rather than slower and faster frame sequences.

Video-based Cardiac Measurement. Diffuse reflections from the body vary depending on how much light is absorbed in the peripheral layers of the skin and this is influenced by the volume of blood in the capillaries. Digital cameras can capture these very subtle changes in light which can then be used to recover the

3 Optical Basis

We start by providing an optical basis for the measurement of the pulse wave using a camera and specifically the second derivative signal. Starting with Shafer’s Dichromatic Reflection Model (DRM)[47,6,23], we want to understand how higher order changes in the blood volume pulse impact pixel intensities to motivate the design of our inputs and loss function. Based on the DRM model the RGB values captured by the cameras as given by:

$$\mathbf{C}_k(t) = I(t) \cdot (\mathbf{v}_s(t) + \mathbf{v}_d(t)) + \mathbf{v}_n(t) \quad (1)$$

where $I(t)$ is the luminance intensity level, modulated by the specular reflection $\mathbf{v}_s(t)$ and the diffuse reflection $\mathbf{v}_d(t)$. Quantization noise of the camera sensor is captured by $\mathbf{v}_n(t)$. $I(t)$ can be decomposed into stationary and time-varying parts $\mathbf{v}_s(t)$ and $\mathbf{v}_d(t)$ [47]:

$$\mathbf{v}_d(t) = \mathbf{u}_d \cdot d_0 + \mathbf{u}_p \cdot p(t) \quad (2)$$

where \mathbf{u}_d is the unit color vector of the skin-tissue; d_0 is the stationary reflection strength; \mathbf{u}_p is the relative pulsatile strengths caused by hemoglobin and melanin absorption; $p(t)$ represents the physiological changes. Let us assume for simplicity in this case that the luminance, I (i.e., illumination in the video) is constant, not time varying, which is a reasonable assumption for short videos and those in which the subject can control their environment (e.g., indoors). Then differentiating twice with respect to time, t :

$$\frac{\partial^2 \mathbf{C}_k(t)}{\partial t^2} = I \cdot \left(\frac{\partial^2 \mathbf{v}_s(t)}{\partial t^2} + \frac{\partial^2 \mathbf{u}_d}{\partial t^2} + \frac{\partial^2 \mathbf{u}_p(t)}{\partial t^2} + \frac{\partial^2 \mathbf{v}_n(t)}{\partial t^2} \right) \quad (3)$$

The non-time varying part $\mathbf{u}_d \cdot d_0$ becomes zero. Thus simplifying the equation to:

$$\frac{\partial^2 \mathbf{C}_k(t)}{\partial t^2} = I \cdot \left(\frac{\partial^2 \mathbf{v}_s(t)}{\partial t^2} + \frac{\partial^2 \mathbf{u}_p(t)}{\partial t^2} + \frac{\partial^2 \mathbf{v}_n(t)}{\partial t^2} \right) \quad (4)$$

Furthermore, if specular reflections do not vary over time (e.g., if the camera and subject are stationary), the $\mathbf{v}_s(t)$ term will also become zero. This means that the second derivative changes in pixel intensities are a sum of second derivative changes in PPG and camera noise. With current camera technology, and little video compression, image noise is typically much smaller than the PPG signal. Therefore, we would expect the pixel changes to be dominated by second derivative variations in the blood volume pulse:

$$\frac{\partial^2 \mathbf{C}_k(t)}{\partial t^2} = I \cdot \frac{\partial^2 \mathbf{u}_p(t)}{\partial t^2} \quad (5)$$

As such, we can infer that when attempting to estimate the second derivative of the PPG signal from videos without very large motions or illumination changes, second derivative changes in the pixel space would appear helpful and that minimizing the loss between the second derivative prediction and ground truth will be the simplest learning task for the algorithm when the input is second-derivative pixel changes.

4 Experimental Architecture

To test our hypothesis we incorporate higher-order dynamics into a model both as inputs and via the loss function. Our goal is to see if they will provide a better estimation of the lower-/higher-order dynamics of the target signal. Convolutional models are the most commonly applied to the task of remote PPG measurement (e.g., [7,39,51,30,21,32]). Our goal here is not to introduce a new network architecture, but rather to systematically analyze the effect of multi-derivative inputs and outputs (see Fig. 2). We perform experiments with two neural architectures: convolutional neural network (CNN) + recurrent neural network (RNN) [30] and a convolutional attention network (CAN) + RNN [6,31]. The main difference between the two is a soft-attention mask in CAN that helps segment the subject from the background and focus on relevant spatial regions. In both cases, we use architectures with a branch for each derivative.

The first-derivative branch extracts features from the differences between consecutive video frames, and similarly the second-derivative branch extracts features from the difference-of-difference frames. In the case of the CAN model, the attention branch uses the raw video frames to learn attention masks (one per frame) that encourage the network to prioritize regions of the image that contain useful signal (e.g. participant’s skin) and ignore noisy regions (e.g. background). These attention masks are shared between the first-derivative branch and the second-derivative branch as we expect the same spatial regions to contain first and second derivative information. After feature representations are extracted from frames within each derivative-input branch, the features are concatenated together for each time step and the target signals are then generated using recurrent neural network (RNN) layers. A high-level diagram depicting the architecture used for our experimentation is shown in Fig. 2. See the supplementary material for a more detailed network architecture diagram.

4.1 Predicting multi-derivative target signals

The goal of iPPG is to obtain an estimate of the underlying PPG signal $p(t)$ (as in Eq. 2), while only observing video frames $X(t)$ containing a subject’s skin (in this case the face). Mathematically, this can be described as learning a function: $\hat{p}(t) = f(X(t))$ or, because we are interested in changes in blood volume changes, estimating the first derivative of the PPG signal: $\hat{p}'(t) = f(X(t), X'(t))$ where the first derivative PPG signal is defined as: $p'(t) = p(t) - p(t-1)$. Using prior methods, to obtain an estimate of the PPG signal’s second derivative, one would either differentiate the predicted PPG signal twice, or differentiate the predicted first-derivative PPG once, rather than calculate the acceleration PPG directly. In contrast, we explicitly predict the acceleration PPG waveform as a target signal. We define the second derivative waveform as the difference between consecutive first-derivative time points: $p''(t) = p'(t) - p'(t-1)$. Then we train our model to predict the second derivative waveform $\hat{p}''(t) = f(X(t), X'(t))$ given a set of input video frames $X(t)$ and the corresponding normalized difference

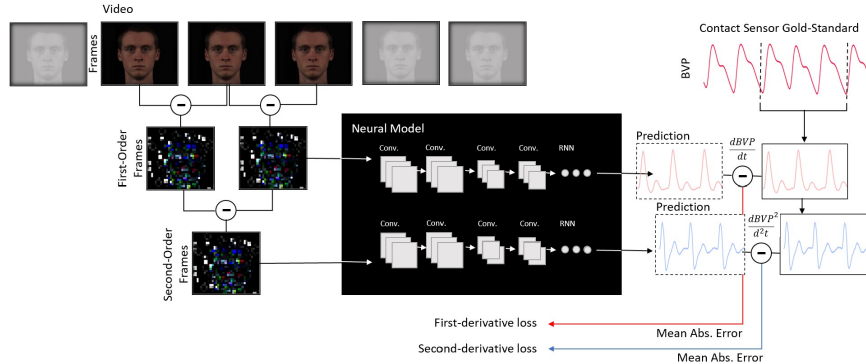


Fig. 2. Our multi-derivative architecture used for experimentation. Spatial features are extracted separately for each set of derivative frames using 3D convolutional layers and mean pooling layers. Once feature representations are extracted, the temporal features from each branch are concatenated together and recurrent layers are used for modeling the temporal signals. The first- and second-derivative losses are calculated as the mean absolute error between the predictions and the synchronized ground-truth PPG signal.

frames $X'(t)$. To optimize our model parameters we minimize the mean squared difference between the true and predicted second derivative waveforms:

$$L = \frac{1}{T} \sum_{t=1}^T (p''(t) - \hat{p}''(t))^2 \quad (6)$$

4.2 Leveraging multi-derivative inputs

It has been previously shown that the normalized difference frames are useful for predicting the first derivative PPG waveforms. Therefore, we hypothesized that incorporating the second derivative of the raw video frames $X''(t) = X'(t) - X'(t-1)$ (i.e. the difference-of-difference frames) may also be useful for predicting the PPG signal and its derivatives. Similar to the difference frames, we added a separate convolutional attention branch, where the attention mask is shared between both branches (see Fig. 2). Sharing the attention mask is a reasonable assumption as we would expect skin regions to all exhibit the signal and similar dynamics. After the feature maps in each branch are pooled into a single value per feature at each time step, the learned representations are concatenated together. These concatenated features over time are used as input sequences to the recurrent layers that generate the target waveforms.

Given that difference frames $X'(t)$ are useful for predicting the first derivative PPG waveforms, features learned from the difference-of-difference frames $X''(t)$ may be beneficial for predicting the second derivative PPG signal. In theory, if difference-of-difference features are indeed useful for predicting the acceleration PPG, then the CAN network should be able to learn those features from the

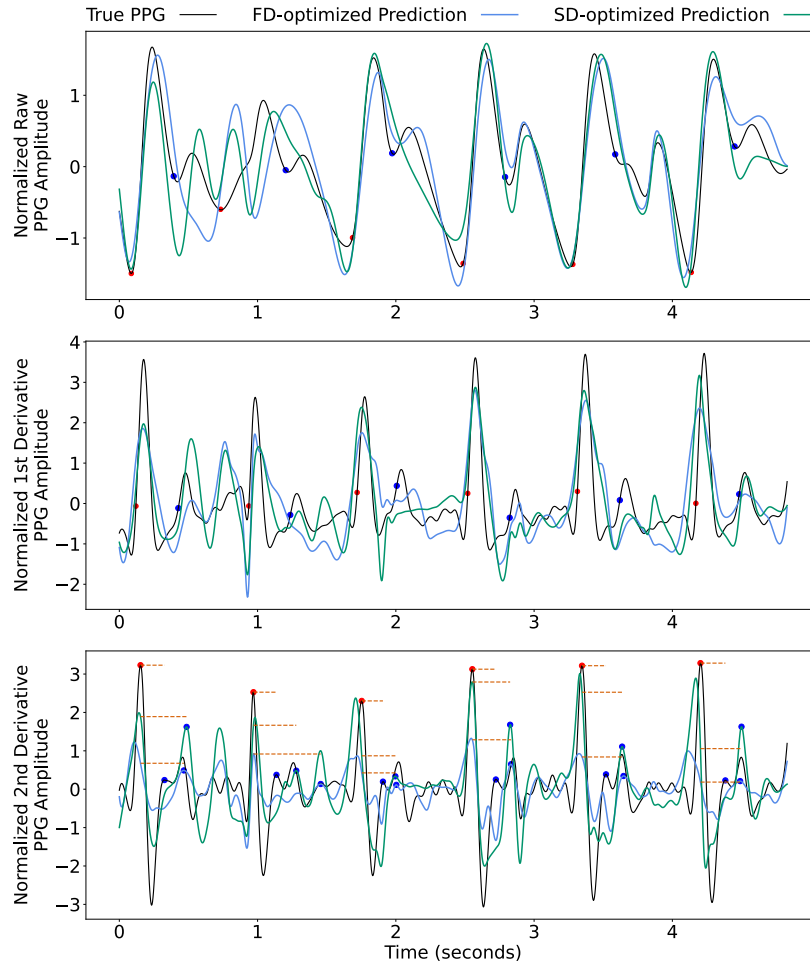


Fig. 3. Comparison of true (*black*) and predicted (*blue and green*) raw or zeroth order (*top*), first order derivative (*middle*), and second order derivative (*bottom*) waveforms. The blue and green lines reflect two models: predicting the first derivative (*blue*) and predicting the second derivative (*green*). Diastolic points are labeled with red dots, and dicrotic notches are labeled with blue dots. LVET intervals are labeled by dotted red lines. Notice how the points of interest are generally more obvious in the second derivative waveforms, as they are maxima rather than inflections. Also note that the LVET time intervals for the second derivative model are generally more similar to those from the contact (true) PPG.

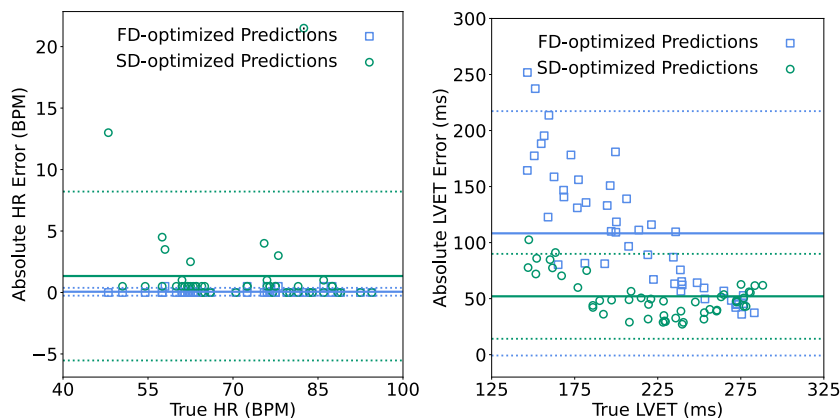


Fig. 4. Bland-Altman plots comparing error distributions for average task heart rate (*left*) and LVET intervals (*right*) for the model optimized for first-derivative prediction (blue) and the model optimized for second-derivative prediction (*green*). (*left*) The absolute difference between the true and predicted heart rate for each subject/task. (*right*) The absolute difference between the predicted and true values (*y-axis, in milliseconds*) is plotted as a function of the true LVET (*x-axis, in milliseconds*). The solid line represents the mean error, and the dotted lines represent the 95% confidence intervals ($\pm 1.96 \times \text{standard deviation}$).

difference frames due to the 3D convolutional operations. However, manually adding the difference-of-difference frames could help guide the model. To examine the effect of combining higher-order inputs and target signals, we fit a model $\hat{p}''(t) = f(X(t), X'(t), X''(t))$ to predict the second-derivative PPG.

5 Experiments

In this section we will describe the data used in our experiments to perform a systematic ablation study in which we test different combinations of inputs and outputs.

5.1 Data

Training To train our models using a large and diverse set of subjects, we leverage recent work that uses highly-parameterized synthetic avatars to generate videos containing simulated subjects with various movements and backgrounds [28]. To drive changes in the synthetic avatars’ appearance, the PPG signal is used to manipulate the base skin color and the subsurface radius [28]. The subsurface scattering is spatially weighted using an artist-created subsurface scattering radius texture that captures variations in the thickness of the skin



Fig. 5. (*left*) Example video frames of different synthetic avatars generated for the training data set. The highly-parameterized avatar generation pipeline enables the creation of diverse subjects with varied demographics, lighting conditions, backgrounds, clothing/accessories, and movements. (*center*) Example video frames from the AFRL testing data set [12] and (*right*) example video frames from the UBFC testing data set [5].

across the face. Using physiological waveform signals from the MIMIC Physionet [15] database, we randomly sampled windows of PPG waveforms from real patients. The physiological waveform data were sampled to maximize examples from different patients. Using the synthetic avatar pipeline and MIMIC waveforms, we generated 2,800 6-second videos, where half of the videos were generated using hand-crafted facial motion/action signals, and the other half using facial motion/action signals extracted using landmark detection on real videos. Examples of the avatars can be found in Fig. 5.

Testing Given that we are focusing on recovering very subtle changes in pixel intensities due to the blood volume pulse, we use a highly controlled and very accurately annotated dataset of real videos for evaluation. The AFRL dataset [12] consists of 300 videos from 25 participants (17 male and 8 female). Each video in the dataset has a resolution of 658x492 pixels sampled at 30 Hz. Ground truth PPG signals were recorded using a contact reflective PPG sensor attached to the subject’s index finger. Each participant was instructed to perform three head motion tasks including rotating the head along the horizontal axis, rotating the head along the vertical axis, and rotating the head randomly once every second to one of nine predefined locations. Since our goal in this work was to compare methods for estimating subtle waveform dynamics, which can be more difficult to do in the presence of large motion, we focused here on the first two AFRL tasks where participant motion is minimal. Examples of AFRL participants can be found in Fig. 5.

5.2 Implementation details

We trained our models using a large dataset of generated synthetic avatars and evaluated model performance on the AFRL dataset, which consists of real human subjects. For each video, we first cropped the video frames so that the face was approximately centered. Next, we reduced the resolution of the video

Table 1. Quantitative cross-dataset performance comparison between different architecture configurations on the AFRL dataset. Models were trained using only the synthetic dataset. Values shown are (mean \pm standard deviation). Beats-per-minute (BPM); First Derivative (FD); Heart Rate (HR); Mean Absolute Error (MAE); Second Derivative (SD); Left Ventricle Ejection Time (LVET).

RhythmNet [30]	Input Frames		Target Signals		HR MAE (BPM)	LVET MAE (ms)
	FD	SD	FD	SD		
(FD-Optimized)	✓	✗	✓	✗	1.82 \pm 6.65	90.82 \pm 48.13
	✓	✗	✓	✓	3.90 \pm 11.39	48.48 \pm 17.34
	✓	✗	✗	✓	2.77 \pm 8.48	49.09 \pm 19.56
	✓	✓	✓	✗	2.35 \pm 7.95	85.69 \pm 43.93
	✓	✓	✓	✓	6.09 \pm 14.27	54.48 \pm 24.42
(SD-Optimized)	✓	✓	✗	✓	4.17 \pm 8.79	54.06 \pm 22.46
CAN [7]						
(FD-Optimized)	✓	✗	✓	✗	0.66 \pm 2.07	108.26 \pm 56.19
	✓	✗	✓	✓	1.63 \pm 4.21	64.77 \pm 31.04
	✓	✗	✗	✓	1.68 \pm 4.85	57.29 \pm 22.68
	✓	✓	✓	✗	0.88 \pm 2.75	75.41 \pm 43.47
	✓	✓	✓	✓	1.16 \pm 3.67	65.99 \pm 31.88
(SD-Optimized)	✓	✓	✗	✓	3.41 \pm 8.77	52.07 \pm 19.53

to 36x36 pixels to reduce noise and computational requirements while maintaining useful spatial signal [45,48,35]. The input to the attention branch was T raw video frames. The input to the first-derivative branch was a set of T normalized difference frames, calculated by subtracting consecutive frames and normalizing by the sum. The input to the second-derivative branch was a set of $T - 1$ difference-of-difference frames (second derivative frames), calculated by subtracting consecutive normalized difference frames (i.e. the T frames used as input to the motion branch). In our experiments, we used a window size of $T = 30$ video frames to predict the target signals for the corresponding 30 time points. During training, a sliding window of 15 frames (i.e. 50% overlap between consecutive windows) was used to increase the total number of training examples. The model was implemented using Tensorflow [1] and trained for eight epochs using the Adam [20] optimizer with a learning rate of 0.001, and a batch size of 16.

5.3 Systematic Evaluation

To measure the effect of using multi-derivative inputs and outputs, we systematically removed the second-derivative parts of the model and used quantitative and qualitative methods to examine the change in model performance. To quantitatively measure the quality of the predicted signal, we calculated two clinically

Table 2. Quantitative cross-dataset performance comparison between different architecture configurations in two separate external datasets using the CAN model: UBFC [5] and PURE [40]. Models were trained only on the synthetic dataset. Descriptions of the FD-optimized and SD-optimized models can be found in Table 1. Values shown are (mean \pm standard deviation).

Beats-per-minute (BPM); First Derivative (FD); Heart Rate (HR); Mean Absolute Error (MAE); Second Derivative (SD); Left Ventricle Ejection Time (LVET).

Model	UBFC		PURE	
	HR MAE (BPM)	LVET MAE (ms)	HR MAE (BPM)	LVET MAE (ms)
(FD-Optimized)	3.59 \pm 9.84	80.90 \pm 58.99	4.17 \pm 2.99	75.84 \pm 18.74
(SD-Optimized)	3.88 \pm 9.85	41.90 \pm 15.72	4.18 \pm 3.26	37.85 \pm 3.57

important parameters - heart rate (HR) and the left ventricular ejection time (LVET) interval (see Appendix A.1 for details). Video-based HR prediction has been a major focus of iPPG applications, with many methods showing highly-accurate results. HR can be determined through peak detection or by determining the dominant frequency in the signal (e.g. using fast Fourier transform). Since current iPPG methods are able to achieve sufficiently-low error rates on the HR estimation task, we believe that metrics that capture the quality of waveform morphology should also be considered.

The LVET interval is defined as the time between the opening and closing of the heart’s aortic valve, i.e. the systolic phase when the heart is contracting (see Fig. 1). In the PPG waveform, this interval begins at the diastolic point (i.e. the global minimum pressure within a heartbeat cycle) and ends with the dicrotic notch (i.e. local minimum occurring after systolic peak, marking the end of the systolic phase and the beginning of the diastolic phase). LVET typically is correlated with cardiac output (stroke volume \times heart rate)[17], and has been shown to be an indicator of future heart failure as the time interval decreases with left-ventricle dysfunction [4].

Calculating LVET requires identification of the diastolic point and the dicrotic notch. The diastolic point is a (global) minimum point within a heart beat, meaning it corresponds to a positive peak in the second derivative signal according to the second-derivative test. Similarly, the dicrotic notch is a (local) minimum in the PPG signal, and appears as a positive peak in the second derivative following the diastolic peak in time. Because the dicrotic notch can often be a subtle feature, it is much easier to identify in the PPG’s second derivative compared to the raw signal. Therefore, it is a good example of clinically-important waveform morphology that is best captured by higher-order dynamics.

What is the impact of first-/second-derivative inputs? In Table 1, quantitative evaluation metrics (HR and LVET) are shown for all experiments in our ablation study, using tasks 1 and 2 from the AFRL dataset. Removing

the second-derivative (SD) frames results in the model configurations in the top three rows of Table 1. When SD frames are removed, the result is a general decrease in the HR error. However, there is also an overall increase in LVET interval prediction error, which suggests that including the SD frames leads to improved estimation of waveform morphology.

What is the impact of a first-/second-derivative loss? Intuitively, models that are optimized using a loss function specifically focusing on a single objective will perform better in terms of that objective compared to models trained with loss functions containing multiple objectives. By removing the first-derivative target signal from the training objective, the model is focused to exclusively focus on the second-derivative (SD) objective. Empirically, this leads the SD-Optimized model to have the lowest LVET MAE of any model configuration (last row of Table 1). While the SD-Optimized model achieves the lowest LVET error, the HR error is the highest of any configuration. These results suggest that there are performance trade-offs to consider when designing a system for particular downstream tasks.

When the second-derivative target signal is removed from the model, the optimization procedure is purely focused on improving the prediction of the first derivative. The FD-Optimized model (first row of Table 1) serves as a form of baseline, since previous works have focused on using first-derivative (FD) frames to predict the first-derivative PPG signal. Fig. 4 shows a Bland-Altman plot [26] comparing the FD-Optimized and SD-Optimized error distributions as a function of the ground-truth values both HR and LVET intervals.

Perhaps unsurprisingly, our results show the FD-Optimized model achieves the lowest HR MAE (0.66 ± 2.07 BPM) of any model configuration examined and, in particular, improves HR estimation compared to models without the first derivative target signal. However, the FD-Optimized model also has the worst performance in terms of the LVET MAE (108.26 ± 56.19 ms) of any model configuration. This suggests that while the configuration provides an accurate assessment of the heartbeat frequency, the quality of predicted waveform morphology can be improved by incorporating second-derivative information.

For a qualitative comparison, in Fig. 3 we plot the ground-truth, FD-Optimized, and SD-Optimized PPG, first derivative, and second derivative. Additionally, in the bottom panel of Fig. 3 we overlay the true and predicted LVET intervals for each signal to demonstrate model performance.

Is performance consistent across architectures? Both the RhythmNet [30] and CAN [7] models show similar trends in results. Models with FD inputs and FD targets show the best HR estimation performance (1.82 and 0.66 BPM for RhythmNet and CAN respectively) (see Table 1).

Is performance consistent across datasets? Results across the AFRL [12], UBFC [5] and PURE [40] datasets show that SD-optimized models consistently provide lower LVET errors (see Table 2) and generally higher HR estimation errors.

6 Conclusions

Using the task of video-based cardiac measurement we have shown that when learning representations for dynamical systems that appropriately designing inputs, and optimizing for derivatives of interest can make a significant difference in model performance. Specifically, there is a trade-off between optimizing for lower-order and higher-order dynamics. Given the importance of second-derivatives (i.e., acceleration) in this, and many other video understanding tasks, we believe it is important to understand the trade-off between optimizing for targets that capture different dynamic properties. In cardiac measurement in particular, the LVET is one of the more important clinical parameters and can be better estimated using higher-order information. While we have investigated the importance of higher-order dynamics in the context of video-based cardiac measurement, this paradigm is generally applicable. We believe future work will continue to showcase the importance of explicitly incorporating higher-order dynamics.

7 Ethics Statement

Camera-based cardiac measurement could help improve the quality of remote health care, as well as enable less invasive measurement of important physiological signals. The COVID-19 pandemic has revealed the importance of tools to support remote care. These needs are likely to be particularly acute in low-resource settings where distance, travel costs, and time are a great barrier to access quality healthcare. However, given the non-contact nature of the technology, it could also be used to measure personal data without the knowledge of the subject. Just as is the case with traditional contact sensors, it must be made transparent when these methods are being used, and subjects should be required to consent before physiological data is measured or recorded. There should be no penalty for individuals who decline to be measured. New bio-metrics laws can help protect people from unwanted physiological monitoring, or discrimination based on pre-existing health conditions detected via non-contact monitoring. However, social norms also need to be constructed around the use of this technology. In this work, data were collected under informed consent from the participants.

References

1. Abadi, M., Agarwal, A., Barham, P., Brevdo, E., Chen, Z., Citro, C., Corrado, G.S., Davis, A., Dean, J., Devin, M., Ghemawat, S., Goodfellow, I., Harp, A., Irving, G., Isard, M., Jia, Y., Jozefowicz, R., Kaiser, L., Kudlur, M., Levenberg, J., Mane, D., Monga, R., Moore, S., Murray, D., Olah, C., Schuster, M., Shlens, J., Steiner, B., Sutskever, I., Talwar, K., Tucker, P., Vanhoucke, V., Vasudevan, V., Viegas, F., Vinyals, O., Warden, P., Wattenberg, M., Wicke, M., Yu, Y., Zheng, X.: TensorFlow: Large-Scale Machine Learning on Heterogeneous Distributed Systems. arXiv:1603.04467 [cs] (Mar 2016), <http://arxiv.org/abs/1603.04467>, arXiv: 1603.04467
2. Annis, T., Pleasants, S., Hultman, G., Lindemann, E., Thompson, J.A., Billecke, S., Badlani, S., Melton, G.B.: Rapid implementation of a COVID-19 remote patient monitoring program. *Journal of the American Medical Informatics Association* **27**(8), 1326–1330 (Aug 2020). <https://doi.org/10.1093/jamia/ocaa097>, <https://doi.org/10.1093/jamia/ocaa097>
3. Bent, B., Goldstein, B.A., Kibbe, W.A., Dunn, J.P.: Investigating sources of inaccuracy in wearable optical heart rate sensors. *npj Digital Medicine* **3**(1), 1–9 (Feb 2020). <https://doi.org/10.1038/s41746-020-0226-6>, <https://www.nature.com/articles/s41746-020-0226-6>, number: 1 Publisher: Nature Publishing Group
4. Biering-Sørensen, T., Querejeta Roca, G., Hegde, S.M., Shah, A.M., Claggett, B., Mosley, T.H., Butler, K.R., Solomon, S.D.: Left Ventricular Ejection Time is an Independent Predictor of Incident Heart Failure in a Community based Cohort. *European journal of heart failure* **20**(7), 1106–1114 (Jul 2018). <https://doi.org/10.1002/ejhf.928>, <https://www.ncbi.nlm.nih.gov/pmc/articles/PMC6685547/>
5. Bobbia, S., Macwan, R., Benezeth, Y., Mansouri, A., Dubois, J.: Unsupervised skin tissue segmentation for remote photoplethysmography. *Pattern Recognition Letters* **124**, 82–90 (Jun 2019). <https://doi.org/10.1016/j.patrec.2017.10.017>, <https://www.sciencedirect.com/science/article/pii/S0167865517303860>
6. Chen, W., McDuff, D.: DeepPhys: Video-based physiological measurement using convolutional attention networks. In: *Proceedings of the European Conference on Computer Vision (ECCV)*. pp. 349–365 (2018)
7. Chen, W., McDuff, D.: DeepPhys: Video-Based Physiological Measurement Using Convolutional Attention Networks. arXiv:1805.07888 [cs] (Aug 2018), <http://arxiv.org/abs/1805.07888>, arXiv: 1805.07888
8. Chen, W., McDuff, D.: DeepMag: Source-Specific Change Magnification Using Gradient Ascent. *ACM Transactions on Graphics* **40**(1), 2:1–2:14 (Sep 2020). <https://doi.org/10.1145/3408865>, <https://doi.org/10.1145/3408865>
9. Dasari, A., Prakash, S.K.A., Jeni, L.A., Tucker, C.S.: Evaluation of biases in remote photoplethysmography methods. *npj Digital Medicine* **4**(1), 1–13 (Jun 2021). <https://doi.org/10.1038/s41746-021-00462-z>, <https://www.nature.com/articles/s41746-021-00462-z>, bandiera_abtest: a Cc.license.type: cc.by Cg.type: Nature Research Journals Number: 1 Primary_atype: Research Publisher: Nature Publishing Group Subject_term: Biomarkers;Developing world Subject_term_id: biomarkers;developing-world
10. Edison, A., Jiji, C.: Optical acceleration for motion description in videos. In: *Proceedings of the IEEE Conference on Computer Vision and Pattern Recognition Workshops*. pp. 39–47 (2017)

11. Elgendi, M., Fletcher, R., Liang, Y., Howard, N., Lovell, N.H., Abbott, D., Lim, K., Ward, R.: The use of photoplethysmography for assessing hypertension. *npj Digital Medicine* **2**(1), 60 (Jun 2019). <https://doi.org/10.1038/s41746-019-0136-7>, <https://doi.org/10.1038/s41746-019-0136-7>
12. Estep, J.R., Blackford, E.B., Meier, C.M.: Recovering pulse rate during motion artifact with a multi-imager array for non-contact imaging photoplethysmography. In: 2014 IEEE International Conference on Systems, Man, and Cybernetics (SMC). pp. 1462–1469 (Oct 2014). <https://doi.org/10.1109/SMC.2014.6974121>, ISSN: 1062-922X
13. Feichtenhofer, C., Fan, H., Malik, J., He, K.: Slowfast networks for video recognition. In: Proceedings of the IEEE/CVF international conference on computer vision. pp. 6202–6211 (2019)
14. Gawalko, M., Duncker, D., Manninger, M., van der Velden, R.M., Hermans, A.N., Verhaert, D.V., Pison, L., Pisters, R., Hemels, M., Sultan, A., Steven, D., Gupta, D., Heidebuchel, H., Schaib, A., Wijtvliet, P., Tieleman, R., Gruwez, H., Chun, J., Schmidt, B., Kearney, J.J., Müller, P., Lodziński, P., Svennberg, E., Hoekstra, O., Jansen, W.P., Desteghe, L., de Potter, T., Tomlinson, D.R., Neubeck, L., Crijns, H.J., Pluymaekers, N.A., Hendriks, J.M., Linz, D., the TeleCheck-AF investigators: The European TeleCheck-AF project on remote app-based management of atrial fibrillation during the COVID-19 pandemic: centre and patient experiences. *EP Europace* **23**(7), 1003–1015 (Jul 2021). <https://doi.org/10.1093/europace/euab050>, <https://doi.org/10.1093/europace/euab050>
15. Goldberger Ary L., Amaral Luis A. N., Glass Leon, Hausdorff Jeffrey M., Ivanov Plamen Ch., Mark Roger G., Mietus Joseph E., Moody George B., Peng Chung-Kang, Stanley H. Eugene: PhysioBank, PhysioToolkit, and PhysioNet. *Circulation* **101**(23), e215–e220 (Jun 2000). <https://doi.org/10.1161/01.CIR.101.23.e215>, <https://www.ahajournals.org/doi/full/10.1161/01.cir.101.23.e215>
16. Greenhalgh, T., Knight, M., Inada-Kim, M., Fulop, N.J., Leach, J., Vindrola-Padros, C.: Remote management of covid-19 using home pulse oximetry and virtual ward support. *BMJ* **372**, n677 (Mar 2021). <https://doi.org/10.1136/bmj.n677>, <https://www.bmj.com/content/372/bmj.n677>, publisher: British Medical Journal Publishing Group Section: Practice
17. Hamada, M., Hiwada, K., Kokubu, T.: Clinical significance of systolic time intervals in hypertensive patients. *European Heart Journal* **11 Suppl I**, 105–113 (Dec 1990)
18. Hill, B.L., Liu, X., McDuff, D.: Beat-To-Beat Cardiac Pulse Rate Measurement From Video. pp. 2739–2742 (2021), https://openaccess.thecvf.com/content/ICCV2021W/V4V/html/Hill_Beat-To-Beat_Cardiac_Pulse_Rate_Measurement_From_Video_ICCVW_2021_paper.html
19. Inoue, N., Kawakami, H., Yamamoto, H., Ito, C., Fujiwara, S., Sasaki, H., Kihara, Y.: Second derivative of the finger photoplethysmogram and cardiovascular mortality in middle-aged and elderly Japanese women. *Hypertension Research* **40**(2), 207–211 (Feb 2017). <https://doi.org/10.1038/hr.2016.123>, <https://www.nature.com/articles/hr2016123>
20. Kingma, D.P., Ba, J.: Adam: A Method for Stochastic Optimization. arXiv:1412.6980 [cs] (Jan 2017), <http://arxiv.org/abs/1412.6980>, arXiv: 1412.6980
21. Lee, E., Chen, E., Lee, C.Y.: Meta-rppg: Remote heart rate estimation using a transductive meta-learner. In: European Conference on Computer Vision. pp. 392–409. Springer (2020)

22. Lewandowska, M., Rumiński, J., Kocejko, T., Nowak, J.: Measuring pulse rate with a webcam — A non-contact method for evaluating cardiac activity. In: 2011 Federated Conference on Computer Science and Information Systems (FedCSIS). pp. 405–410 (Sep 2011)
23. Liu, X., Fromm, J., Patel, S., McDuff, D.: Multi-task temporal shift attention networks for on-device contactless vitals measurement. arXiv preprint arXiv:2006.03790 (2020)
24. Liu, Z., Ning, J., Cao, Y., Wei, Y., Zhang, Z., Lin, S., Hu, H.: Video swin transformer. arXiv preprint arXiv:2106.13230 (2021)
25. Lu, H., Han, H., Zhou, S.K.: Dual-gan: Joint bvp and noise modeling for remote physiological measurement. In: Proceedings of the IEEE/CVF Conference on Computer Vision and Pattern Recognition. pp. 12404–12413 (2021)
26. Martin Bland, J., Altman, D.: STATISTICAL METHODS FOR ASSESSING AGREEMENT BETWEEN TWO METHODS OF CLINICAL MEASUREMENT. *The Lancet* **327**(8476), 307–310 (1986). [https://doi.org/10.1016/S0140-6736\(86\)90837-8](https://doi.org/10.1016/S0140-6736(86)90837-8), <http://www.sciencedirect.com/science/article/pii/S0140673686908378>
27. McDuff, D., Gontarek, S., Picard, R.W.: Remote Detection of Photoplethysmographic Systolic and Diastolic Peaks Using a Digital Camera. *IEEE Transactions on Biomedical Engineering* **61**(12), 2948–2954 (Dec 2014). <https://doi.org/10.1109/TBME.2014.2340991>, <http://ieeexplore.ieee.org/document/6863634/>
28. McDuff, D., Hernandez, J., Wood, E., Liu, X., Baltrusaitis, T.: Advancing non-contact vital sign measurement using synthetic avatars. arXiv preprint arXiv:2010.12949 (2020)
29. Nister, D., Naroditsky, O., Bergen, J.: Visual odometry. In: Proceedings of the 2004 IEEE Computer Society Conference on Computer Vision and Pattern Recognition, 2004. CVPR 2004. vol. 1, pp. I–I (Jun 2004). <https://doi.org/10.1109/CVPR.2004.1315094>, ISSN: 1063-6919
30. Niu, X., Shan, S., Han, H., Chen, X.: Rhythmnet: End-to-end heart rate estimation from face via spatial-temporal representation. *IEEE Transactions on Image Processing* **29**, 2409–2423 (2019)
31. Nowara, E., McDuff, D., Veeraraghavan, A.: The Benefit of Distraction: Denoising Remote Vitals Measurements using Inverse Attention. arXiv:2010.07770 [cs, eess] (Oct 2020), <http://arxiv.org/abs/2010.07770>, arXiv: 2010.07770
32. Nowara, E.M., McDuff, D., Veeraraghavan, A.: The benefit of distraction: Denoising camera-based physiological measurements using inverse attention. In: Proceedings of the IEEE/CVF International Conference on Computer Vision. pp. 4955–4964 (2021)
33. Pereira, T., Tran, N., Gadhoumi, K., Pelter, M.M., Do, D.H., Lee, R.J., Colorado, R., Meisel, K., Hu, X.: Photoplethysmography based atrial fibrillation detection: a review. *npj Digital Medicine* **3**(1), 1–12 (Jan 2020). <https://doi.org/10.1038/s41746-019-0207-9>, <https://www.nature.com/articles/s41746-019-0207-9>
34. Poh, M.Z., McDuff, D.J., Picard, R.W.: Advancements in noncontact, multiparameter physiological measurements using a webcam. *IEEE transactions on biomedical engineering* **58**(1), 7–11 (2010)
35. Poh, M.Z., McDuff, D.J., Picard, R.W.: Non-contact, automated cardiac pulse measurements using video imaging and blind source separation. *Optics Express* **18**(10), 10762–10774 (May 2010). <https://doi.org/10.1364/OE.18.010762>,

- <https://www.osapublishing.org/oe/abstract.cfm?uri=oe-18-10-10762>, publisher: Optical Society of America
36. Reisner, A., Shaltis, P., McCombie, D., Asada, H., Warner, D., Warner, M.: Utility of the Photoplethysmogram in Circulatory Monitoring. *Anesthesiology* **108**(5), 950–958 (May 2008). <https://doi.org/10.1097/ALN.0b013e31816c89e1>, <https://doi.org/10.1097/ALN.0b013e31816c89e1>
 37. Rohmetra, H., Raghunath, N., Narang, P., Chamola, V., Guizani, M., Lakkani, N.R.: AI-enabled remote monitoring of vital signs for COVID-19: methods, prospects and challenges. *Computing* (Mar 2021). <https://doi.org/10.1007/s00607-021-00937-7>, <https://doi.org/10.1007/s00607-021-00937-7>
 38. Song, R., Chen, H., Cheng, J., Li, C., Liu, Y., Chen, X.: PulseGAN: Learning to generate realistic pulse waveforms in remote photoplethysmography. *IEEE Journal of Biomedical and Health Informatics* **25**(5), 1373–1384 (2021)
 39. Špetlík, R., Franc, V., Matas, J.: Visual heart rate estimation with convolutional neural network. In: *Proceedings of the British Machine Vision Conference*, Newcastle, UK. pp. 3–6 (2018)
 40. Stricker, R., Müller, S., Gross, H.M.: Non-contact video-based pulse rate measurement on a mobile service robot. In: *The 23rd IEEE International Symposium on Robot and Human Interactive Communication*. pp. 1056–1062 (Aug 2014). <https://doi.org/10.1109/ROMAN.2014.6926392>, iSSN: 1944-9437
 41. Takano, C., Ohta, Y.: Heart rate measurement based on a time-lapse image. *Medical engineering & physics* **29**(8), 853–857 (2007)
 42. Takazawa, K.: Clinical usefulness of the second derivative of a plethysmogram (acceleration plethysmogram). *J Cardiol* **23**, 207–217 (1993)
 43. Takazawa, K., Tanaka, N., Fujita, M., Matsuoka, O., Saiki, T., Aikawa, M., Tamura, S., Ibukiyama, C.: Assessment of Vasoactive Agents and Vascular Aging by the Second Derivative of Photoplethysmogram Waveform. *Hypertension* **32**(2), 365–370 (Aug 1998). <https://doi.org/10.1161/01.HYP.32.2.365>, <https://www.ahajournals.org/doi/10.1161/01.HYP.32.2.365>
 44. Takeda, S., Okami, K., Mikami, D., Isogai, M., Kimata, H.: Jerk-aware video acceleration magnification. In: *Proceedings of the IEEE Conference on Computer Vision and Pattern Recognition*. pp. 1769–1777 (2018)
 45. Verkruyse, W., Svaasand, L.O., Nelson, J.S.: Remote plethysmographic imaging using ambient light. *Optics express* **16**(26), 21434–21445 (2008)
 46. Virtanen, P., Gommers, R., Oliphant, T.E., Haberland, M., Reddy, T., Cournapeau, D., Burovski, E., Peterson, P., Weckesser, W., Bright, J., van der Walt, S.J., Brett, M., Wilson, J., Millman, K.J., Mayorov, N., Nelson, A.R.J., Jones, E., Kern, R., Larson, E., Carey, C.J., Polat, I., Feng, Y., Moore, E.W., VanderPlas, J., Laxalde, D., Perktold, J., Cimrman, R., Henriksen, I., Quintero, E.A., Harris, C.R., Archibald, A.M., Ribeiro, A.H., Pedregosa, F., van Mulbregt, P.: *SciPy 1.0: fundamental algorithms for scientific computing in Python*. *Nature Methods* **17**(3), 261–272 (Mar 2020). <https://doi.org/10.1038/s41592-019-0686-2>, <https://www.nature.com/articles/s41592-019-0686-2>, number: 3 Publisher: Nature Publishing Group
 47. Wang, W., den Brinker, A.C., Stuijk, S., De Haan, G.: Algorithmic principles of remote ppg. *IEEE Transactions on Biomedical Engineering* **64**(7), 1479–1491 (2016)
 48. Wang, W., den Brinker, A.C., Stuijk, S., de Haan, G.: Algorithmic Principles of Remote PPG. *IEEE Transactions on Biomedical Engineering* **64**(7), 1479–1491 (Jul 2017). <https://doi.org/10.1109/TBME.2016.2609282>, conference Name: IEEE Transactions on Biomedical Engineering

49. Wu, H.Y., Rubinstein, M., Shih, E., Guttag, J., Durand, F., Freeman, W.: Eulerian video magnification for revealing subtle changes in the world. *ACM transactions on graphics (TOG)* **31**(4), 1–8 (2012)
50. Wu, T., Blazek, V., Schmitt, H.J.: Photoplethysmography imaging: a new noninvasive and noncontact method for mapping of the dermal perfusion changes. In: *Optical Techniques and Instrumentation for the Measurement of Blood Composition, Structure, and Dynamics*. vol. 4163, pp. 62–70. International Society for Optics and Photonics (2000)
51. Yu, Z., Li, X., Zhao, G.: Remote Photoplethysmograph Signal Measurement from Facial Videos Using Spatio-Temporal Networks. arXiv:1905.02419 [cs] (Jul 2019), <http://arxiv.org/abs/1905.02419>, arXiv: 1905.02419
52. Zhang, Y., Pintea, S.L., Van Gemert, J.C.: Video acceleration magnification. In: *Proceedings of the IEEE Conference on Computer Vision and Pattern Recognition*. pp. 529–537 (2017)

A Appendix

A.1 Supplemental Methods

Convolutional Attention Network (CAN) Model Architecture The first two 3D convolutional layers in each branch each have 16 filters and the final two 3D convolutional layers in each branch each have 32 filters. Each convolutional layer has a filter size of 3x3x3 for all 3D convolutional layers in the network. All convolutional layers are padded such that they have the same height, width, and number of time steps in each consecutive layer. Convolutional layers use the hyperbolic tangent activation function, except for the convolutional layers used for the attention masks which use a sigmoid activation function for generating the soft masks. Attention masks (one per time step) are applied by applying an element-wise multiplication of the attention mask with each 3D convolutional feature map. Average pooling layers reduce the height and width of the frames by a factor of two, except for the final average pooling layer that pools over the entire frame (i.e. reduces each feature map to a single value per time step). Dropout (25% probability) is applied after every pooling layer to reduce overfitting.

After the final pooling layer, the learned features for each time step in a branch are concatenated together (i.e. combined across branches to share information). Each target signal uses its own set of (2) RNN layers to read the concatenated features over time and generate a target sequence. The first RNN layer is implemented as a bi-directional GRU (hyperbolic tangent activation function) with 64 total units (32 each direction). The second RNN layer is a GRU (linear activation function) layer with 1 output value per time step.

RhythmNet-based Model Architecture We use a CNN+RNN model architecture based on the RhythmNet [30] architecture, where the CNN layers learn to capture spatial signals and the RNN layers then map the features over time into a BVP signal. The model implementation is very similar to the CAN model architecture, but without the attention mechanism (see previous section for description). Fig. 6 depicts the model architecture used, with one branch per input frame type. For the models that only include first derivative frames, a single branch is used and therefore the branches are not concatenated together.

Metric Calculation

Heart Rate (HR) estimation To estimate the heart rate, we use an fast Fourier transform (FFT)-based method to calculate the dominant frequency in the signal, which corresponds to the heart rate. We first estimate power spectral density using the “periodogram” function from the `scipy.signal` [46] library. Then we band-pass filter the PPG signal, with cutoff frequencies of 0.75-4.0 Hz (corresponding to a minimum HR of 45 BPM and maximum HR of 240 BPM). Finally, we select the frequency with the maximum power, and use this as our estimated HR.

Left Ventricle Ejection Time (LVET) estimation The LVET time is defined as the time interval between the diastolic peak and the dicrotic notch.

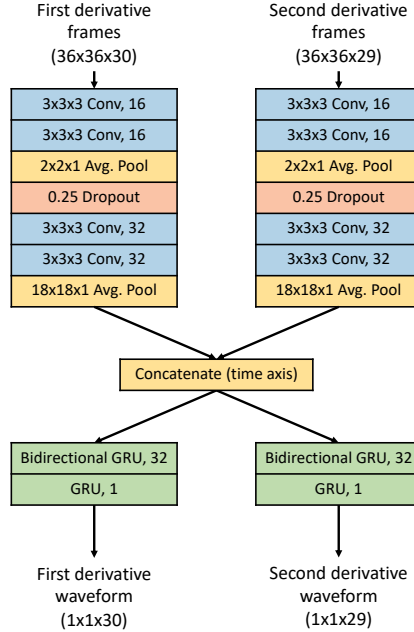


Fig. 6. CNN+RNN model based on the Rhythm-Net architecture [30]. For model architecture configurations that only use the FD frames, only the left branch is used and therefore the concatenation layer is not needed.

To calculate this interval, we first identified the diastolic point in the second derivative (SD) of the PPG signal, which, because it is a “global” minima in the PPG heartbeat, appears as a “global” maxima (positive SD value) in the SD PPG. Then, in each predicted SD PPG waveform, we identified candidate diastolic notch points. Since the diastolic notch manifests as a “local” minima in the PPG signal, it appears as a “local” maxima in the PPG SD signal (positive SD value). Using peak detection (“find_peaks” function in the `scipy.signal` library [46]) we identify candidate diastolic notch points by finding local peaks that occur after a diastolic point, and use the diastolic notch candidate point that is closest in time to the reference diastolic point.

Because both the ground truth PPG (and therefore its derivatives) and, in particular, the predicted PPG (and its derivatives), contain signal artifacts and noise, the peak detection process is not perfect. To reduce variability in the LVET interval estimates due to noise, we apply a smoothing operation. Specifically, we estimate the mean LVET interval within a 10-second non-overlapping

window and use this as our estimate of true/predicted LVET. See Appendix Fig. 7 for example LVET intervals over time, and the estimated LVET intervals after smoothing within windows.

A.2 Supplemental Results

Table 3. Quantitative performance comparison between different architecture configurations using the CAN model. Values shown are (mean \pm standard deviation). Beats-per-minute (BPM); First Derivative (FD); Heart Rate (HR); Mean Absolute Error (MAE); Second Derivative (SD); Left Ventricle Ejection Time (LVET).

Input Frames		Target Signals		HR MAE (BPM)	LVET MAE (ms)
FD	SD	FD	SD		
✗	✓	✓	✗	3.14 ± 7.07	83.09 ± 42.41
✗	✓	✓	✓	6.97 ± 16.30	65.10 ± 31.56
✗	✓	✗	✓	2.95 ± 6.57	57.67 ± 25.82

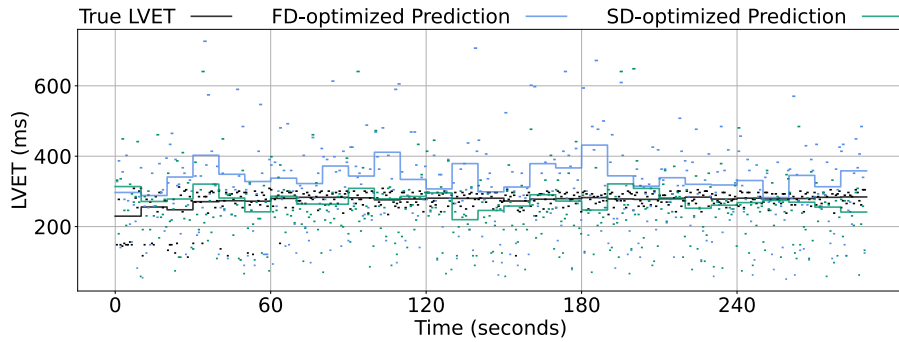


Fig. 7. Comparison of Left Ventricle Ejection Time (LVET) estimation over a 5-minute time period. Solid lines are computed as the mean LVET interval within non-overlapping 10-second windows.